Article

Laminar Boundary Layer over a Serrated Backward-Facing Step

Real J. KC [1], Trevor C. Wilson [1], Nicholas A. Lucido [2], Aaron S. Alexander [3], Jamey D. Jacob [1] and Brian R. Elbing [1,*]

[1] Mechanical and Aerospace Engineering, Oklahoma State University, Stillwater, OK 74078, USA; realk@okstate.edu (R.J.K.); trevor.wilson@okstate.edu (T.C.W.); jdjacob@okstate.edu (J.D.J.)

[2] Mechanical Engineering, University of Michigan, Ann Arbor, MI 48109, USA; nalucido@umich.edu

[3] Mechanical Engineering Technology, Oklahoma State University, Stillwater, OK 74078, USA; aaral@okstate.edu

* Correspondence: elbing@okstate.edu

Abstract: Laminar flow over a modified backward-facing step (BFS) was studied experimentally and computationally, with the results compared to a flight test on a Piper Cherokee wing. The BFS was modified with a serrated spanwise variation while maintaining a constant step height, and this modification is termed a serrated BFS (sBFS). A scaling law was proposed and then used to develop the experimental operation conditions. The experiments showed evidence that the transition to turbulence was delayed over the forward part of the serration (termed the valley). The boundary layer growth and characterization were used to validate the computational model, which was then used to examine details not available from the experiment, including the wall shear stress distribution and streamlines as they go over the sBFS. The wall shear stress showed the formation of low-shear diamonds downstream of the sBFS valley that were associated with laminar flow, which confirmed previous assumptions about the low-shear diamonds observed in the flight tests. The length of the low-shear diamonds was scaled with the sBFS geometry. Finally, the streamlines showed that the near-wall flow forward of the sBFS is pumped towards the sBFS peak, where it rapidly transitions to turbulence at that location.

Keywords: flow control; backward-facing step; passive; CFD; drag

1. Introduction

Surface disturbances (e.g., rivets, skin joints, blemishes) cause a wide variety of adverse flow phenomena, including flow separation. Some applications that are commonly impacted by such disturbances include airplanes, automobiles, wide-angle diffusers, and combustors [1,2]. For aircraft, flow separation on the wing can cause a reduction in lift in addition to increased pressure drag [3]. While such disturbances cause an adverse effect in both laminar and turbulent flows, the current work focuses on the laminar flow regime. More specifically, the current work aims at mitigating the adverse effects of a laminar boundary layer over a backward-facing step (BFS).

A BFS is a geometric discontinuity that has been studied for many years [4]. BFS flows are a canonical flow that is used in a multitude of numerical and experimental studies. The majority of BFS studies focus on turbulent flow (e.g., [5]) due to many applications operating in that regime. However, there are several studies focused on laminar BFS flows. For example, Armaly et al. [6] studied the spanwise velocity distribution and reattachment length, and Steinhorsson et al. [7] investigated the impact of sidewalls on bounded BFS experiments. In spite of the relative dearth of laminar BFS studies, there are common applications involving laminar flow over a BFS. One major application is the use of a protective film on the leading edge of airfoils, where the flow has not yet transitioned to turbulent flow. While the film protects the airfoil, the BFS that is created by the tape is detrimental to the performance of the airfoil [8–10].

Control of the flow aft of a BFS can broadly be divided between active and passive flow control methods [11]. Active flow control adds energy to the system to manipulate the flow characteristics, which requires drag reduction to break even for energy savings and often significantly increases complexity. Consequently, passive flow control that typically involves geometric modifications is commonly used. The primary issue with passive flow control methods is that they generally have a narrow operation range and cannot be "turned off" like active methods when outside of that operation range. Vortex generators (VG) are one of the most common passive flow control devices and are designed for specific flow regimes [12]. For example, VGs such as the Gurney flap are designed for low angles of attack [13], while other designs can operate at high angles of attack [14]. These passive flow control devices, such as VGs, reenergize the boundary layer and delay the laminar-to-turbulence transition. Fransson et al. [15] showed that the transition to turbulence in a boundary layer can be delayed by using well-designed surface roughness. Shahinfar et al. [16] also showed that the transition to turbulent flow can be delayed using miniature VGs. They showed that the disturbance energy inside the boundary layer can be reduced by three orders of magnitude. In a more recent study, Siconolfi et al. [17] explore the idea of inducing free stream vortices to alter the boundary layer stability characteristics that may delay the transition to turbulent flow. Additionally, passive methods exist for mitigating shockwave-induced boundary layer separation in the supersonic regime [18], the elimination of flap separation of take-off and landing configurations, an increasing lift-to-drag ratio at various angles of attack [19], noise reduction [20], and the reduction of drag induced by shockwaves on transonic aircraft wings [21,22]. The shockwave-induced drag for transonic aircraft has been achieved with 3D bumps [21] as well as with a three-dimensional serrated pattern BFS [22]. While the transonic results from previous studies are promising, please note that the current study is only applicable to subsonic flight.

The serrated backward-facing step (sBFS) investigated in the current study has shown promise in mitigating adverse effects created by BFSs and other flow disturbances. Most previous reports have referred to this specific geometry as a conformal vortex generator (CVG). One of the most promising sBFS applications is the mitigation of the adverse effects from the use of protective films applied to the leading edge of wind turbines. The degradation of the leading edge of wind turbines is a major issue that significantly impacts the performance of the wind turbine [23]. To mitigate this, a thin layer of protective tape is typically applied to the leading edge. While this protects the blade, the addition of the tape creates a backward-facing step that can be detrimental to the performance of the wind turbine. In recent studies, Major et al. [8,9] concluded that the addition of leading-edge protective tape increases the C_d of the blade by up to 62%, which can potentially result in losses of 2–3% in terms of annual energy production. The National Renewable Energy Laboratory (NREL) compared wind turbine performance with the standard protective film that has a straight BFS to that of the sBFS used in the current study [24]. Preliminary results showed an increase in the wind turbine performance of up to 7.4% when using sBFS compared to the standard film. This observation motivated the study by KC et al. [25], which experimentally and computationally investigated the bulk flow modifications induced by sBFS on an airfoil shape. That study showed that the sBFS could reduce drag relative to a standard BFS by up to 8–10%. In addition, wake surveys showed that the sBFS could produce strong coherent structures that persisted into the far wake region. These sBFS patterns have also been investigated in other flow applications, including the aft of the slat step on a Boeing 737 wing [22], on helicopter blades, and on a Piper Cherokee wing [22,26].

The flight test results from the Piper Cherokee wing [22,26] was the primary motivation for the current study. The main measurement from those flight tests was the visualization of the wall shear stress using a biphenyl solution on the wing. For each flight, a light-colored crystalline biphenyl solution was applied to sections of the wing that were previously painted black to create a sharp contrast. The rate that the solution was removed from the wing was dependent on the amount of shear force being applied. Consequently, regions

of low shear would remain light colored longer than regions of high shear, where the biphenyl solution was removed, leaving the black paint. Figure 1 compares a before and after image from the flight tests reported in Kibble [22]. An interesting observation from these flight tests was the formation of a diamond shaped region of lower shear immediately downstream of the sBFS. The length and width of the sBFS on these flight tests were varied, resulting in changes in the length of these low-shear diamonds.
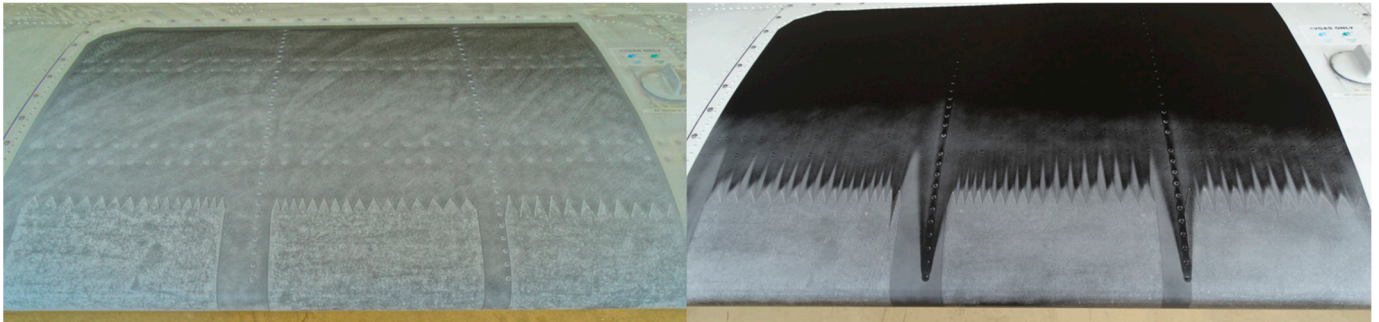

Figure 1. Images adapted from Kibble [22] showing (**left**) before and (**right**) after flight tests on a Piper Cherokee wing, with light regions in the after indicating relatively lower shear.

It was proposed that the low-shear diamonds are associated with a delay in the laminar-to-turbulent transition; however, there is little detail about the induced flow pattern. Consequently, the current study investigates these low-shear diamonds observed on the flight scale tests downstream of the sBFS. This is initially approached by proposing a scaling law to design a water tunnel experiment matching the nominal flight scale conditions. Then, the experimental data were used to validate a computational model, which provided detailed measurements of the wall shear stress distribution and the flow pattern induced by the sBFS. The experimental and computational methods are described in Section 2, the results are presented in Section 3, the results are analyzed and discussed in Section 4, and finally, conclusions are summarized in Section 5.

2. Methodology

2.1. Scaling Law

A proposed working model for this problem, illustrated in Figure 2, assumes that the velocity field downstream of the sBFS ($\vec{u}_d$) depends on the inlet boundary layer, sBFS geometry (step height H, width W, and length L), and the fluid properties (density ρ and kinematic viscosity ν). The laminar inlet boundary layer can be characterized by the boundary layer thickness (δ), freestream speed (U_∞), and local pressure gradient (dp/dx).

Given the proposed parameter space, a resulting scaling law is

$$\frac{\vec{u}_d}{U_\infty} = \phi\left(\frac{\delta}{H}, \frac{U_\infty H}{\nu}, \frac{H}{\rho U_\infty^2}\frac{dp}{dx}, \frac{W}{H}, \frac{L}{H}\right). \tag{1}$$

This scaling law was used to design the current experiments with the aim of replicating the Piper Cherokee flight tests [22,26]. Several sBFS configurations were flight tested on the Piper Cherokee, but the current experimental design used $H = 0.367$ mm, $W = 17.1$ mm, and $L = 23.5$ mm because this configuration was also examined on the Boeing 737 [22,27]. The Piper Cherokee flight tests were performed at a nominal altitude of 1000 m above sea level with $\rho = 1.11$ kg/m^3 and $\nu = 1.58 \times 10^{-5}$ m^2/s. The flight scale inlet boundary layer is difficult to estimate due to the limited reported information about the operating conditions [22,27]. However, it was estimated that the cruise speed (U_∞) was nominally 70 m/s. The wall shear stress visualization during the flight tests (see Figure 1) provides an indication of the likely boundary layer condition. Specifically, the lower shear regions (i.e., the brighter sections) suggested that the boundary layer was laminar upstream of the

sBFS and then transitioned to turbulent downstream. Thus, an upper bound for the inlet boundary layer thickness would be the Blasius (flat plate, $dp/dx = 0$) laminar boundary layer solution. The Blasius solution estimates the boundary layer thickness to $\delta \approx 1$ mm at the sBFS location. Xfoil [28] was used to refine this estimate to account for the local favorable pressure gradient, which resulted in $\delta \cong 0.693$ mm with $dp/dx \approx -412$ Pa/m.
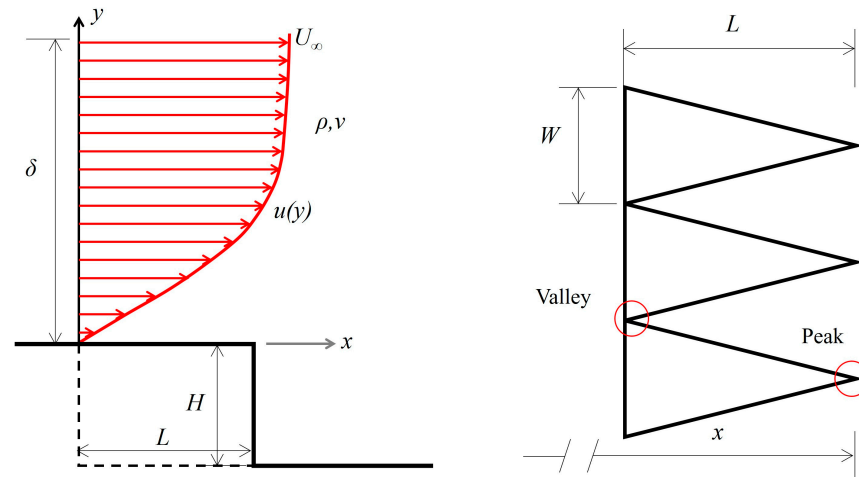
Figure 2. Illustration of the (**left**) side and (**right**) top views of the sBFS step and the working model for the scaling law. As illustrated, the upstream and downstream locations of the backward-facing step are termed the "valley" and "peak," respectively.

Given these flight scale parameters, the independent scaled variables in Equation (1) can be determined, and these flight scale values are listed in Table 1. Patel [29] showed that the log-region of a boundary layer had negligible variation when $K < 1.6 \times 10^{-6}$, where K is defined as

$$K = \frac{\nu}{U_\infty^2} \frac{dU_\infty}{dx}.$$ (2)

Table 1. Nominal independent parameters used in the scaling law provided in Equation (1) for the Piper Cherokee flight test [22,26].

Parameter	Flight Scale Value
δ/H	1.89
Re_H	1620
$\frac{dp}{dx}\frac{H}{\rho U_\infty^2}$	-2.8×10^{-5}
W/H	47
L/H	64
K	1.7×10^{-8}

Using traditional boundary layer assumptions, the pressure gradient is readily written in terms of the streamwise gradient of the freestream speed, $dp/dx = -\rho U_\infty \, dU_\infty/dx$. Substituting this in Equation (2) shows that K is a ratio of two of the independent parameters

$$K = -\frac{\nu}{\rho U_\infty^3} \frac{dp}{dx} = -\left(\frac{dp}{dx} \frac{H}{\rho U_\infty^2}\right)\left(\frac{1}{Re_H}\right),$$ (3)

where $Re_H = U_\infty H/\nu$. The resulting K value $\left(1.7 \times 10^{-8}\right)$ for the flight scale testing is well below this limit, which indicates that the pressure gradient had a negligible impact on the resulting flow field within the flight tests. For this reason, a simple flat plate model was

used for the experiments, though a flap was fabricated for the model to impose a pressure gradient if needed.

2.2. Experimental Methods

The experiments were performed in the flow visualization water tunnel (Model 503, Engineering Lab Design) at Oklahoma State University, as illustrated in Figure 3. This tunnel can achieve speeds up to 1.1 m/s in an unobstructed test section. The test section had acrylic walls for optical access and was 1 m long with a 300 mm square cross section. The flow was driven by two centrifugal pumps controlled by independent variable frequency drives. A flat plate with a 5:1 elliptical leading edge was mounted within the test section. It measured 750 mm (length) × 300 mm (wide) × 12.7 mm (thick). The trailing edge had a flap that could be varied to control the pressure gradient, which for the current study was set close to zero.
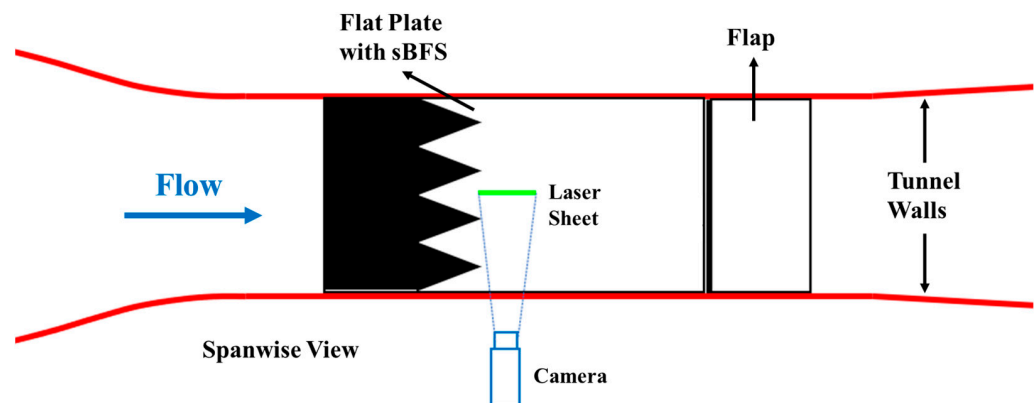

Figure 3. A schematic of the water tunnel used for all experimental testing in this study. The nominal location of the PIV FOV is indicated by the laser sheet location.

To mitigate the impact of surface finish and surface application, it was decided to use the same polyurethane film used in the flight tests. The primary limitation created by this decision was that it required that the model step height (H_m) be an integer multiple (layering) of the thickness supplied by the film manufacturer (Edge Aerodynamix, Wentworth Falls, Australia). The only film thickness (i.e., step height) was $H = 0.367$ mm, which matched the flight scale. Testing was performed in a water tunnel to minimize the number of layers required. With a nominal speed of 1 m/s, this set the step height (i.e., film thickness) equal to four layers of the original film, $H_m = 1.47$ mm. To match the flight-scaled Reynolds number and scaled boundary layer thickness, the freestream speed and boundary layer thickness needed to be 1.1 m/s and $\delta = 2.8$ mm, respectively. Assuming a laminar flat plate (Blasius) boundary layer, the step needed to be located 300 mm downstream. However, the downstream-based Reynolds number for this configuration was 3.8×10^5, which exceeded the laminar-to-turbulent transition Reynolds number (3.5×10^5) for flat plates [30]. This limitation combined with a desire to ensure that an integer number of cycles spanned the tunnel width (valley-to-valley or peak-to-peak) required adjustment of the final experimental conditions. The sBFS was applied with the valley location 300 mm downstream of the leading edge. Each layer was carefully wrapped around the leading edge of the model and extended up to 200 mm downstream from the leading edge on the backside. The width was set at 76 mm, which was slightly larger than that required to match W/H but was set to produce an integer number of cycles in the spanwise direction. The corresponding length of the sBFS was 105 mm. More details about the experimental scaling can be found in Lucido et al. [26].

Two-dimensional, two-component particle image velocimetry (PIV) was performed to investigate the boundary layer behavior downstream of the sBFS. The PIV setup used a pair of Nd:YAG pulsed lasers (Ultra 50, Big Sky Laser Technology, Bozeman, MT, USA) that had a maximum power output of 30 mJ at 532 nm wavelength. The maximum pulse

repetition rate for these lasers was 15 Hz, and the pulse duration was 8 ns. The lasers (and camera) were mounted to a traversing optical table below the test section to enable the field-of-view (FOV) to be readily moved in the streamwise direction. The tunnel was seeded with 18 μm diameter hollow glass spheres (iM30K, 3M, Saint Paul, MI, USA). The camera (Motion Pro X3, Redlake, Woodsville, NH, USA) had a resolution of 1.3 megapixels (1280 × 1024 pixels) and a maximum frame rate at full resolution of 1000 frames per second. The camera was operated in double exposure mode with a 100 ns shutter speed. The camera was equipped with a macro lens (Zoom 7000, Navitar, Rochester, NY, USA). Laser and camera timing/triggering was controlled with a tandem pair of pulse generators (400I, Global Specialist Instruments; Model 9518, Quantum, Bozeman, MT, USA). The first unit controlled overall timing, while the second unit was used as a delay generator. The spacing between images varied from 500 to 1000 μs.

The raw PIV images were imported into a commercial processing software (DaVis 8.2.1, LaVision). A calibration function was generated using 20 images of a 14 × 14 grid with 2.98 mm spacing. A strong linear sharpening filter was applied to the raw calibration images and subsequently averaged. This averaged calibration image was used to create a third-order polynomial calibration function fit. The standard deviation of the calibrated fit was kept below 3 pixels. A square mask was applied to the images so that velocity vectors were only calculated inside this region. Multi-pass processing with a decreasing interrogation window size was used to compute the vector field. After starting with an initial window size of 128 by 128 pixels with 50% overlap, the final interrogation window was 16 by 16 pixels with 75% overlap, which made the final resolution of the PIV data 0.13 mm. Nominally, 340 by 270 vectors were calculated per vector field. Additional processing was performed within a separate commercial software package (MATLAB 2018a, MathWorks).

Wall normal (y) velocity profiles were extracted from the ensemble average of the individual snapshots of the vector field. These profiles were used to identify the boundary layer parameters, including the freestream speed, boundary layer thickness, displacement thickness, momentum thickness, and shape factor. The freestream velocity was determined from averaging velocity measurements well above the boundary layer thickness (i.e., in the region of relatively uniform velocity), for which the variation in the freestream speed was below 3%. Given the freestream speed, the boundary layer height was determined by fitting the velocity profile with a power-law fit and identifying when it achieved 99% of the freestream speed. The momentum and displacement thicknesses were determined from integration of the velocity profiles and their definitions.

The PIV uncertainty was quantified following the method described in Wieneke [31]. This approach uses the computed displacement to transform the raw images to an equivalent time associated with the peak correlation and then slightly shifted (~1 pixel) away from the optimal displacement. Any asymmetry in the shifted correlations is directly related to the level of noise in the image. This analysis showed the uncertainty was below 1%. Standard propagation of uncertainty methods were employed to estimate the uncertainty for other parameters, including the momentum thickness, which had a nominal uncertainty of 0.6%.

Four different freestream velocity conditions (0.1, 0.6, 0.9, and 1.1 m/s) were tested with the sBFS. Due to the limited FOV of the PIV setup, data were recorded at multiple streamwise locations, with each FOV spanning nominally 20 mm in the streamwise direction. A total of 34 locations downstream of the sBFS were recorded. Fourteen sets were collected downstream of both peak and valley spanwise locations, which produced a total streamwise length of 280 mm. The additional six locations were collected downstream of the midpoint between the peak and valley spanwise positions, resulting in a streamwise distance of 120 mm.

2.3. Computational Methods

The experimental results were used to validate a computational model, which was used to examine the shear stress within the region of the diamonds as well as the flow pattern induced by the sBFS. A commercial software package (STAR-CCM+, Siemens, Munich, Germany) was used to create an implicit unsteady computational simulation. The time step size was controlled such that the CFL number was less than unity. The simulation domain is illustrated in Figure 4, with the bottom surface being the flat plate and the sBFS valleys located 150 mm downstream from the domain inlet. PIV measurements were acquired 150 mm upstream of the experimental sBFS, and the interpolation of these PIV results were used as the velocity inlet condition for the simulations. The exit boundary condition was a pressure outlet. The top surface had a slip wall, while the bottom surface (i.e., the plate model) had a no-slip wall. The spanwise (*z*-direction) boundaries were a periodic interface. The dimension of the simulation domain and the fluid properties are given in Table 2.
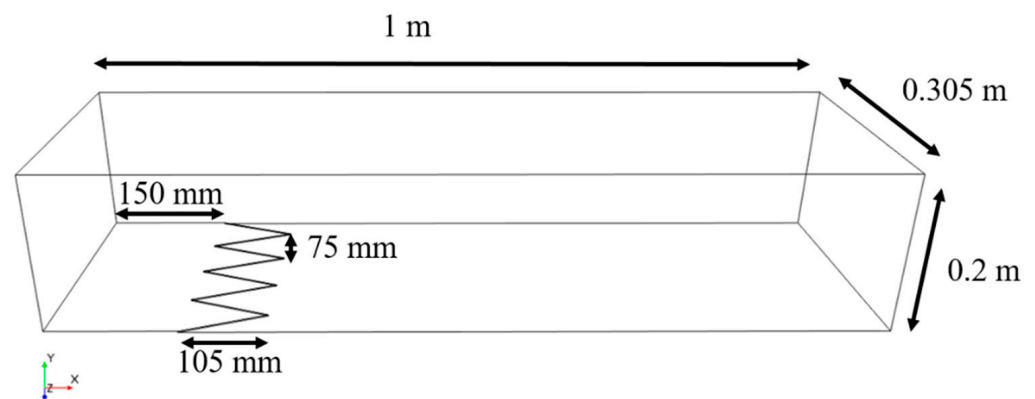

Figure 4. A simulation domain for modeling the sBFS on a smooth flat plate. The flow is from the left to the right, with the sBFS making a 1.5 mm serrated backward-facing step as shown.

Table 2. Geometry and flow properties of water tunnel simulations.

Parameter	Water Tunnel Scale	Units
H	1.5	mm
L	105	mm
W	76	mm
x	300	mm
Volume	$1 \times 0.3 \times 0.305$	m
ρ	998	kg/m^3
μ	9×10^{-4}	Pa·s
U	0.6/0.9/1.15	m/s
δ	2–2.5	mm
Δy	<y+	
Δx	30 y+	
Δz	30 y+	
dt	10^{-4}, 2×10^{-8}	s
Cell count	65	million cells

The mesh for these simulations was built utilizing a commercial mesher (STAR-CCM+'s Advancing layer mesher, Siemens). The mesher generated polyhedral cells along with prism layers in the near-wall regions. Prism layers were crucial for properly resolving the structure within the boundary layer. A cross-section of the mesh is shown in Figure 5. Segregated method was used for all the simulations. Quasi-direct numerical simulation (qDNS) was used as the solver for all simulations in the current study. This solver utilizes the LES model, but the sub-grid scale model is turned off and locally solved with a finer mesh. This was performed based on STAR-CCM+ recommendations [32,33].
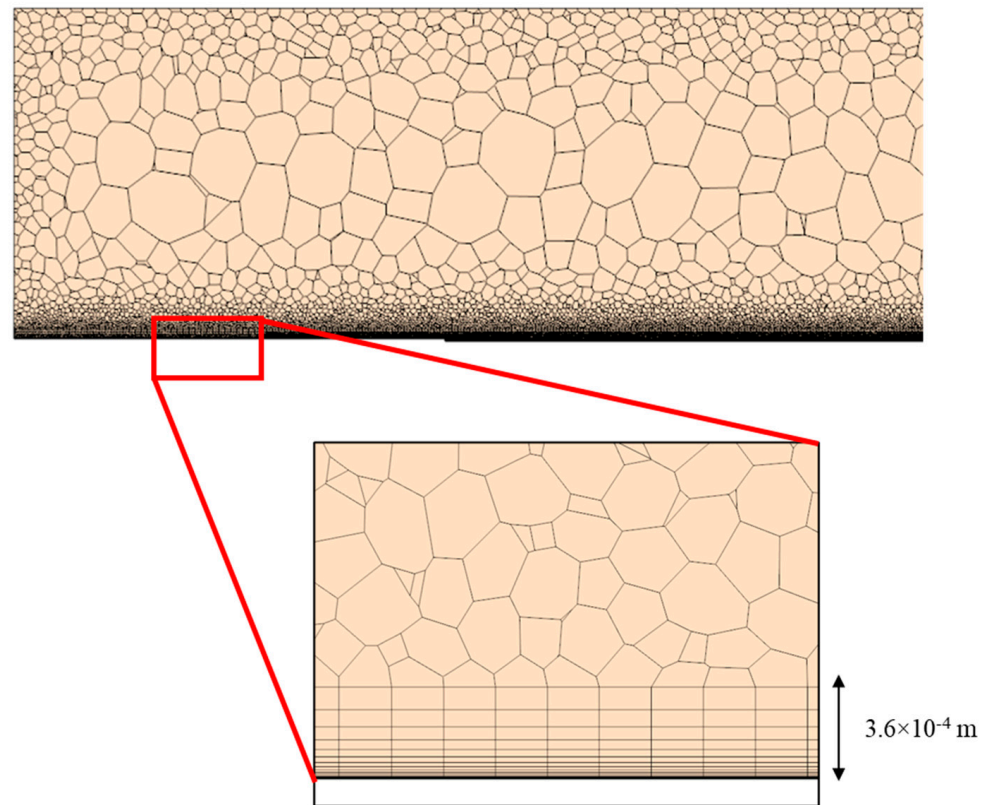
Figure 5. (**top**) A cut out of the mesh in the streamwise direction and (**bottom**) a zoomed-in section of the mesh that shows the prism layers near the wall.

The simulations were run on the Oklahoma State University's High-Performance Computing Center (HPCC), which had two clusters that had 252 and 164 computing nodes, respectively. The run time for a simulation was roughly 10 days, which resulted in the utilization of roughly 150,000 core hours per simulation. Before the computational results were compared with the experiments, the mesh dependence of the solution was analyzed. Table 3 shows the four mesh iterations used to test this dependence with their corresponding shear diamond length (L_d) and boundary layer heights (δ_{99}). Note that these two variables are independent. The δ_{99} columns show the boundary layer height at 3 different locations. The first one is the δ_{99} height at x = 0.1 m from the inlet (i.e., upstream of the sBFS). The second and the third δ_{99} columns show the boundary layer height at x = 0.3 m from the inlet directly downstream of either the valley (x_v) or the peak (x_p) location. The results indicate that the most refined mesh was sufficiently resolved since there was minimal mesh dependence observed between the largest meshes.

Table 3. Values of the shear diamond length (L_d) and boundary layer thickness (δ_{99}) for varying mesh sizes. Note that the variables L_d and δ_{99} are independent. The δ_{99} columns provide the boundary layer height at 3 different locations. The subscripts P and V denote peak and valley spanwise locations, respectively.

Mesh	L_d (m)	δ_{99} (mm)		
		x = 0.1 m	x_V = 0.3 m	x_P = 0.3 m
6,000,000	0.364	4.50	5.10	6.20
12,000,000	0.324	3.90	4.27	5.15
35,000,000	0.327	3.85	4.24	5.10
65,000,000	0.327	3.83	4.25	5.10

3. Results

3.1. Experimental Results

3.1.1. Flat Plate

To confirm that the incoming boundary layer on the test model was laminar, measurements were initially acquired without an sBFS. Measurements were taken at four test speeds ($0.1 \leq U_\infty \leq 1.0$ m/s) and two downstream locations (x = 158 and 370 mm). The streamwise velocity profiles were extracted from the average PIV vector field for each test speed and measurement location. The local freestream speed and boundary layer thickness were measured and used to scale all the velocity profiles (i.e., outer variable scaled) in Figure 6. For reference, the Blasius solution for laminar flat plates is included as well as a 1/7th power-law fit that is a common fit for turbulent profiles. The current data follow the laminar (Blasius) profile much more closely than that of turbulent profiles. For the highest speeds tested and farthest downstream location, the profiles appear to be deviating from the Blasius solution, which suggests that in this range, the flow could be transitional. These initial flat plate measurements were used to confirm that the boundary layer was laminar at the sBFS location.
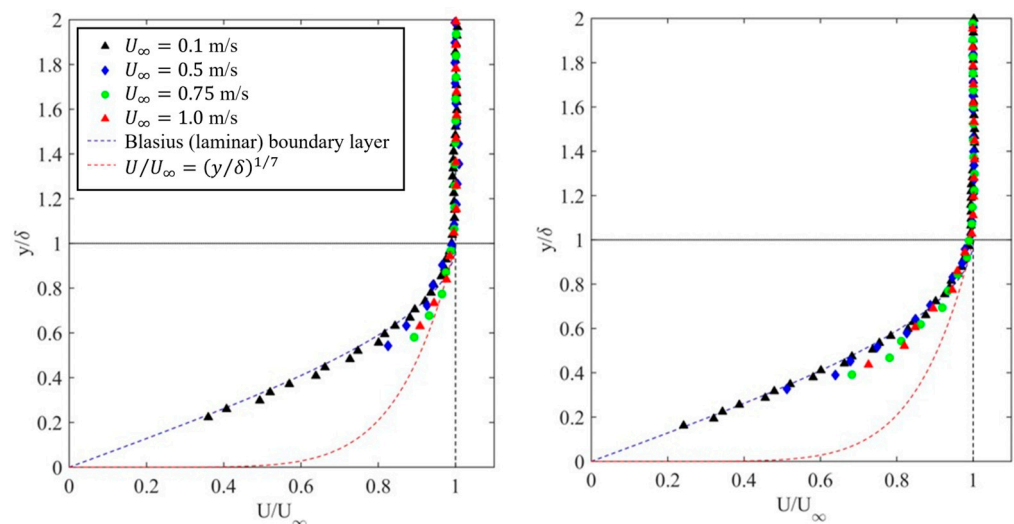

Figure 6. Outer variable scaled streamwise velocity profiles for a flat plate without sBFS applied with at (**left**) x = 158 mm and (**right**) x = 370 mm.

3.1.2. sBFS Model

Figure 7 shows the streamwise velocity field directly downstream of a (left) peak and (right) valley. Note that the step is further upstream for the valley, but the measurement FOV is obstructed by the peak locations between the camera and the measurement plane. Thus, the valley contour plot shown is 105 mm downstream of the valley step. The

contour map for the peak location shows that the profile is initially laminar, but within approximately 30 mm downstream, the profile transitions to turbulent. The valley contour map already appears turbulent at this condition, but for lower speeds ($U_\infty \leq 0.6$ m/s), the profile remained laminar at this downstream location.
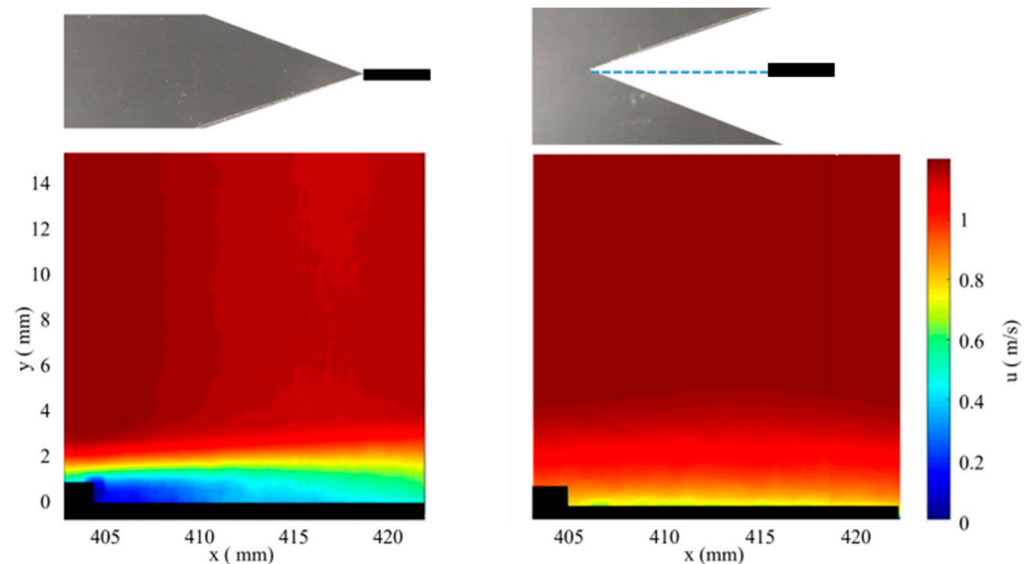

Figure 7. A plot of the streamwise velocity vector field downstream of the (**left**) peak and (**right**) valley location. The illustration above each contour plot marks the measurement location with a black rectangle relative to the sBFS location.

The velocity profiles obtained from PIV were used for a quantitative comparison of the boundary layer evolution. The mean outer variable scaled streamwise velocity profiles 100 mm downstream of the peak location are shown in Figure 8. This shows that at this downstream location, the profiles can be laminar, transitional, or turbulent depending on the speed and spanwise location. The 0.6 m/s condition is of particular interest because it shows that the profile is laminar downstream of the valley (and mid-plane), while downstream of the peak, it is transitioning to turbulent. This is in spite of the fact that the valley step was 100 mm further upstream than the peak. This was the first indication that the low-shear diamonds on the flight test might be due to a delayed transition from laminar to turbulent flow.

The momentum thickness θ and displacement thickness δ^* for each profile was calculated, the ratio of which gives the boundary layer shape factor, δ^*/θ. The shape factor is a convenient parameter for determining if the boundary layer is laminar, turbulent, or transitional. From the Blasius solution, the shape factor for laminar flow is 2.59, while flat plate turbulent boundary layers are nominally 1.3 assuming a 1/7th velocity profile [34]. Figure 9 shows the shape factor versus downstream distance-based Reynolds number for all locations measured. This shows that the lowest test speed (0.1 m/s) was laminar for all test conditions and locations on the model, which is not representative of the target condition. At other velocities, the results show the flow transitioning from laminar to turbulent with an increasing Reynolds number. Specifically, the valley appears to transition to turbulent profiles at a higher Reynolds number than that of the peak. This is consistent with the flight tests that indicated turbulent flow occurred immediately after the peak but not the valley.
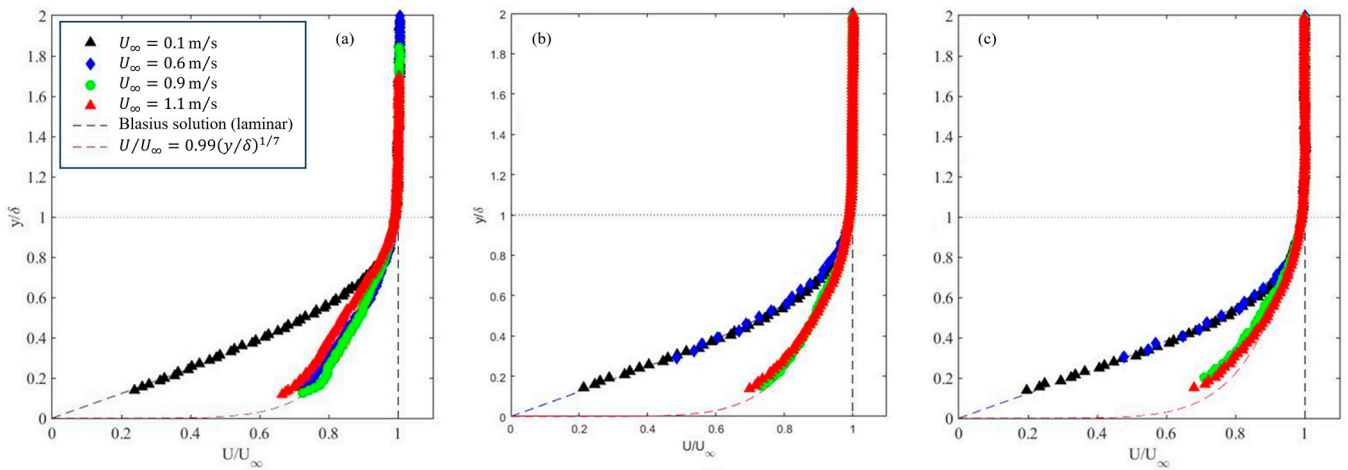
Figure 8. Outer variable scaled streamwise velocity profiles at the spanwise position of the sBFS (**a**) peak, (**b**) midpoint between valley and peak, and (**c**) valley. All measurements were 505 mm downstream of the model leading edge, which is approximately 100 mm downstream of the sBFS peak location.
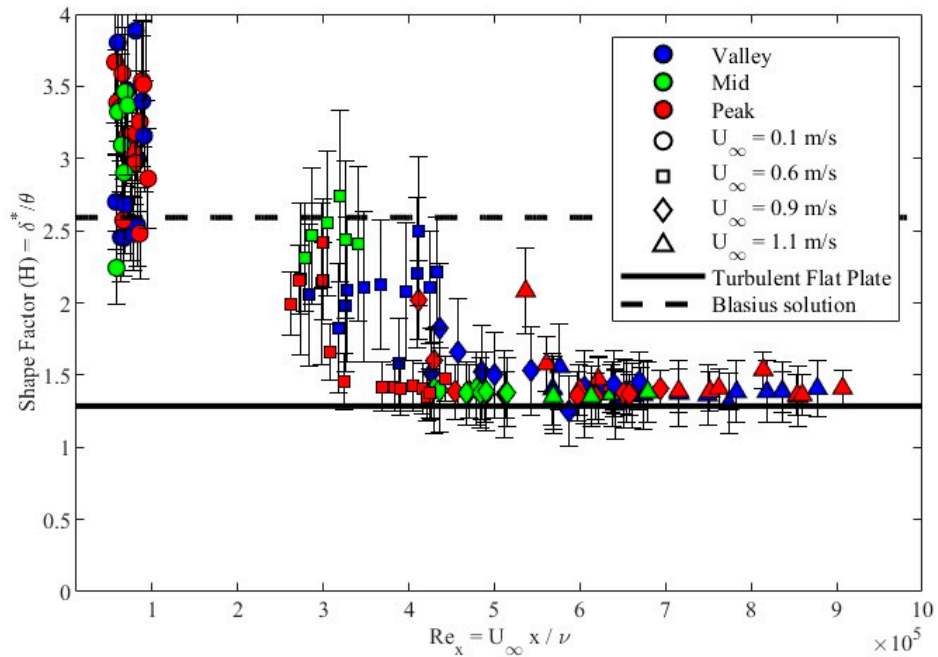

Figure 9. Shape factor plotted versus the downstream distance-based Reynolds number. All data were acquired on a flat plate model downstream of the sBFS. The color indicates the spanwise position (valley, mid, or peak), while the marker shape indicates the test speed. For reference, lines corresponding to the shape factor for turbulent and laminar flat plates are included.

3.2. Computational Results

3.2.1. Flat Plate

The computational results were initially validated on a flat plate with no sBFS. This validation was necessary to ensure that the selected solvers and methods could adequately model a developing boundary layer over a flat plate with the given experimental inlet velocity data. The PIV velocity profile from $x = 158$ mm was used as the inlet condition for the simulation. At this location, the displacement and momentum thickness-based Reynolds numbers were nominally $Re_{\delta*} = 950$ and $Re_{\theta} = 280$. Then, additional PIV velocity profiles at $x = 250$ and 300 mm were used to validate the growth of the boundary layer in the simulation. Once again, the streamwise velocity (u) profiles were scaled

with outer variables (i.e., boundary layer thickness δ and free stream velocity U_∞). The comparison of the experimental and computational velocity profiles is provided in Figure 10, along with the Blasius solution for laminar flat plate boundary layers. This shows that the experimental profile had a slight deviation from the Blasius solution and that the computational results are in excellent agreement with the experimental results. The match of the boundary layer growth between the experimental and computational simulation gives confidence that the computational model was adequately capturing the physics. Thus, the model could be investigated further to give information that was not available from the experiment (e.g., velocity field where the experimental FOV was blocked).
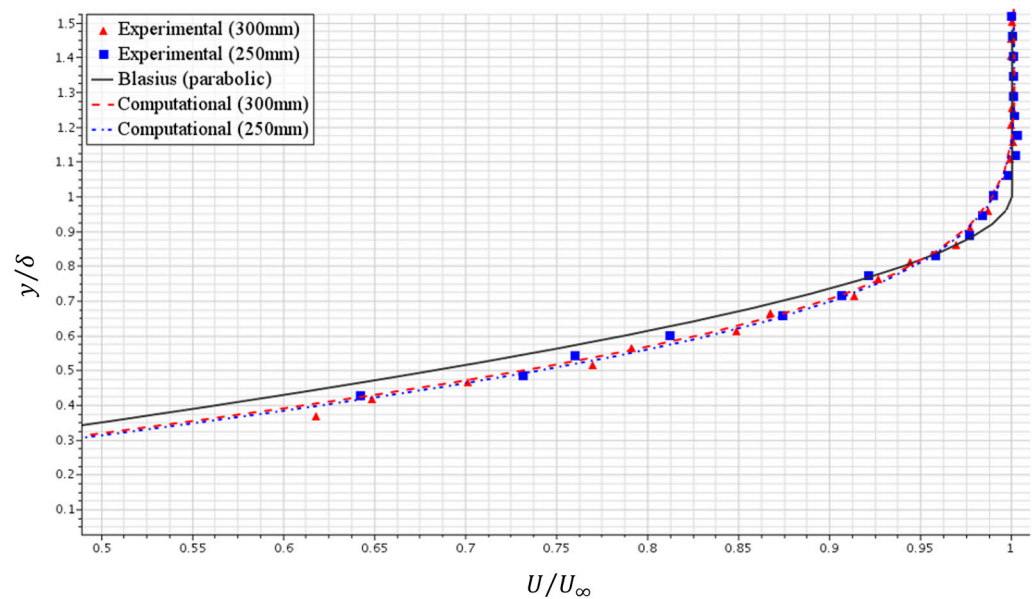
Figure 10. A comparison between the experimental and computational outer variable scaled velocity profiles at 250 mm ($Re_{\delta*} = 1000$) and 350 mm ($Re_{\delta*} = 1100$) downstream on the flat plate without an sBFS.

3.2.2. Flat Plate with sBFS

The sBFS was added to the simulation and compared with the experimental (PIV) results. For the simulations, there were three different inlet conditions ($U_\infty = 0.6, 0.9,$ and 1.15 m/s) tested. For each test speed, the velocity profile from the experiment at $x = 158$ mm was used as the inlet condition for the simulation. Figure 11 shows an example of a comparison of the streamwise velocity downstream of the peak at a speed of 1.1 m/s for PIV and computational results. This shows two of the PIV FOVs compared against the same region for the simulation with a dashed line marking seven step heights downstream as a reference. These results illustrate that the same flow structure was observed on both the experimental and computational models. However, it does appear that the boundary layer thickened more slowly in the simulation than in the experiments. This will be revisited subsequently with a more quantitative analysis.

Without the FOV limitation of the experiment, the flow directly downstream of the valley can be compared with the flow directly downstream of the peak. Figure 12 shows contour plots from the simulation immediately downstream of the peak and valley at a freestream speed of 1.15 m/s. Both cases (peak and valley) have the flow reattach at nominally seven step heights downstream, which is consistent with traditional BFS observations. However, there is a stark difference in the flow structure between the step and the reattachment for the peak and valley locations. The valley has a more linear or convex structure in the reattachment region, while the peak has a more concave structure, which is similar to traditional BFS. Beyond the reattachment point, the two locations also have an apparent difference. Downstream of the reattachment point for the peak has the

flow transition to a turbulent boundary layer, while it remains laminar downstream of the valley.
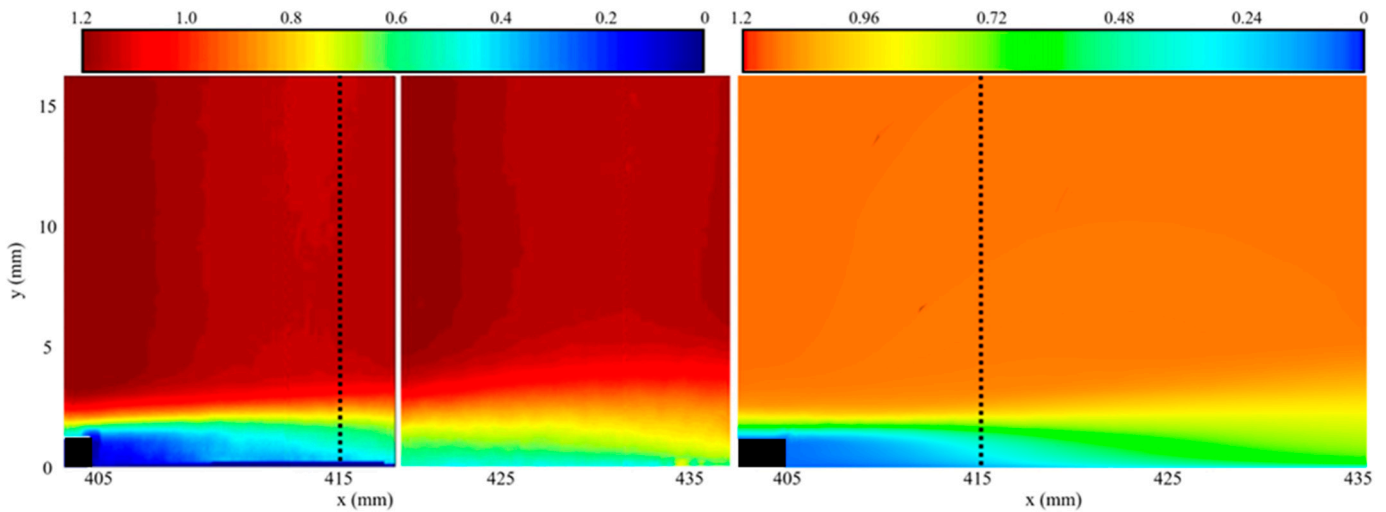

Figure 11. Velocity magnitude downstream of the sBFS peak for the (**left**) experiment and (**right**) simulation. Black dashed lines indicate 7 step heights downstream of the step as a reference. The gap in the experimental data is due to non-overlapping FOVs.
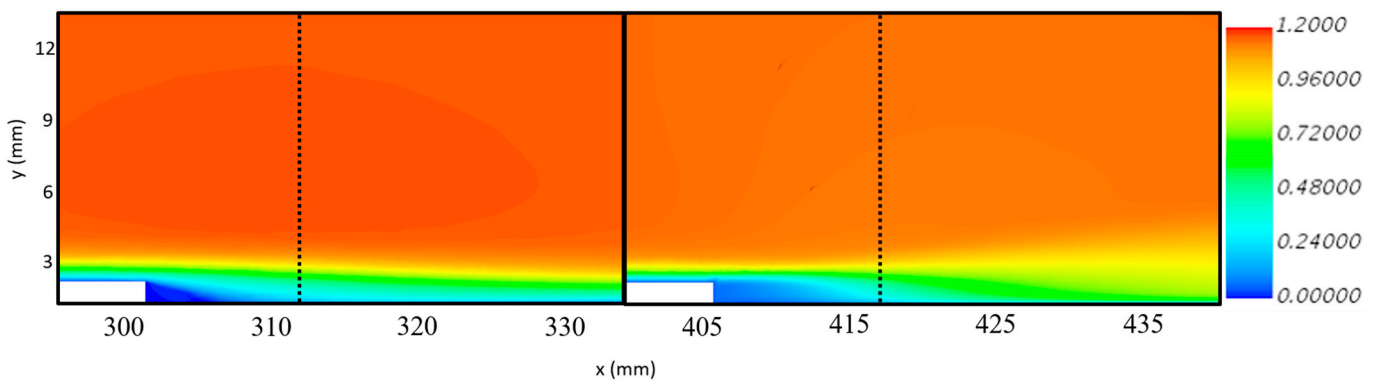

Figure 12. A contour plot of the velocity magnitude from the simulation showing flow immediately downstream of the sBFS at the (**left**) valley and (**right**) peak spanwise locations. Flow is from left to right.

Once again, the shape factor is used to make a more quantitative comparison of the boundary layer evolution over the sBFS. The shape factor versus Reynolds number downstream of the peak and valley for all three simulation test speeds is shown in Figure 13. The experimental results are included to assist with the interpretation of the results and provide guidance on observed differences. These results show that for most conditions, the boundary layer structure was similar between the experiment and simulation. The largest discrepancy was for 0.6 m/s downstream of the valley, for which the experimental data were laminar or transitional over the entire measurement range, even downstream of the peak location. Conversely, the CFD model shows a laminar shape factor from the step to past the peak downstream location, but then, it transitions to a turbulent boundary layer. This is likely related to the fact that in the simulation, there was an exact point of transition, but in the real world, the flow transition is not instantaneous and sensitive to local perturbations. Therefore, while the exact values of the data sets vary, they both showed the transition, which provided evidence that the CFD results were reasonably accurate.
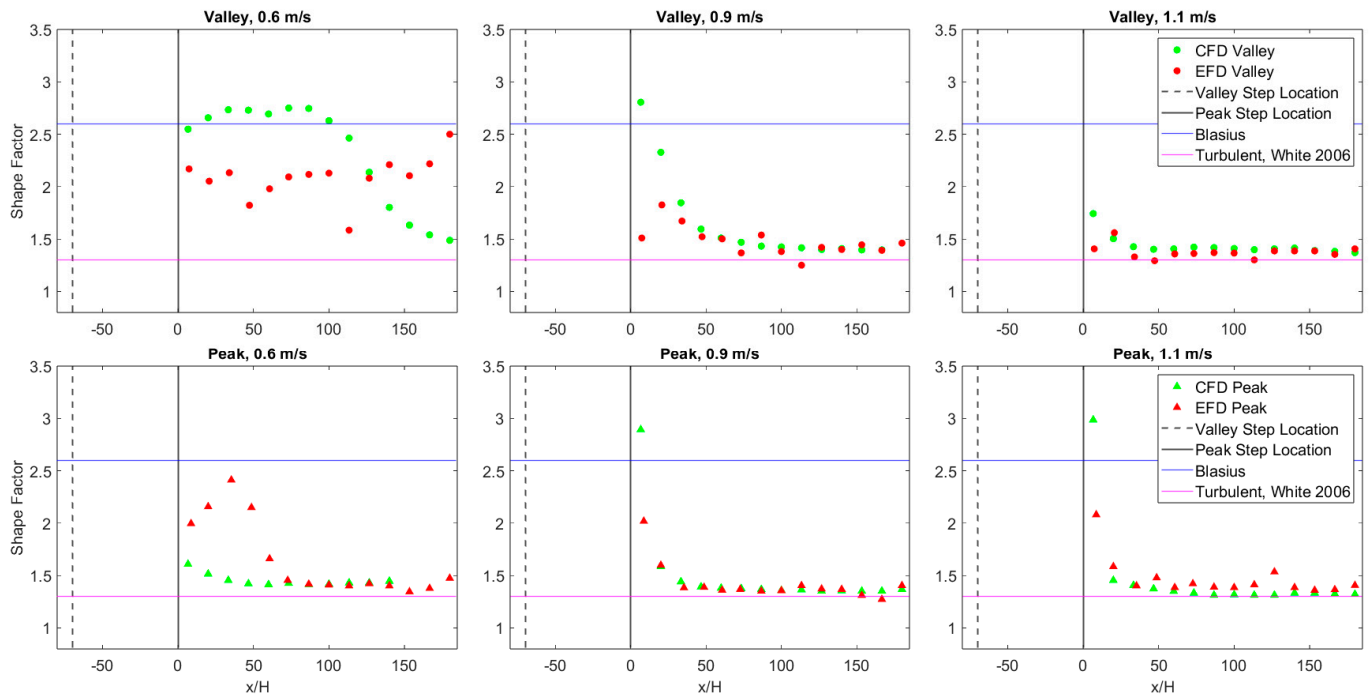
Figure 13. The boundary layer shape factor for the (**top row**) valley and (**bottom row**) peak spanwise locations at inlet speeds of (left to right) 0.6 m/s, 0.9 m/s, and 1.1 m/s. Experimental fluid dynamic (EFD) and computational fluid dynamic (CFD) results are included as well as the Blasius and turbulent solutions [35]. Black lines indicate the location of the valley and peak steps, and the *x*-axis is the downstream distance from the peak (*x*) divided by the step height (*H*).

In addition, Figure 13 shows that for the 0.6 m/s condition, the boundary layer transitioned to turbulent immediately downstream of the step for both data sets. At 0.9 m/s, the shape factor indicates that downstream of the valley, the boundary layer transitioned to a turbulent boundary layer at a small distance downstream of the peak downstream position, while downstream of the peak transitioned immediately. Finally, the 1.15 m/s condition appeared to be turbulent from the peak downstream location for both the peak and valley spanwise locations. In summary, at the tested speeds, the shape factor was affected differently by the peak and the valley. Downstream of the valley, the shape factor transitioned to turbulent flow at different locations based on the speed. However, downstream of the peak, the shape factor indicated a transition for all speeds tested. This resulted in the conclusion that the sBFS was, in fact, imparting spanwise variation in the boundary layer characteristics that was consistent between the experiment and simulation.

4. Discussion

4.1. Extended sBFS CFD Analysis

With verification that the simulation was accurately capturing the impact of the sBFS on the boundary layer development, the CFD model was used to further investigate the details of the flow field that were not available from the experimental results. The first investigation was of the wall shear stress,

$$\tau_w = \mu \left. \frac{du}{dy} \right|_{y=0}, \tag{4}$$

downstream of the sBFS. Specifically, we investigated the region downstream of the valley, where experimentally it could not be observed and where the flight scale showed the low-shear diamonds. The simulated wall shear stress for the three test speeds is shown in Figure 14. The comparison of these wall shear stress contour plots with the shape factor

plots in Figure 13 shows that the low shear downstream of the valley coincides with the location of the laminar boundary layers. In general, the flow downstream of the valley is transitioning to high shear at the same locations where the shape factors were changing, and the shear stress was high past the peaks at all speeds. Thus, these wall shear stress results confirm and extend the shape factor results to the region immediately downstream of the sBFS valleys. This also gives evidence in support of the assumption that the diamonds observed on the flight tests were due to local laminar flow.
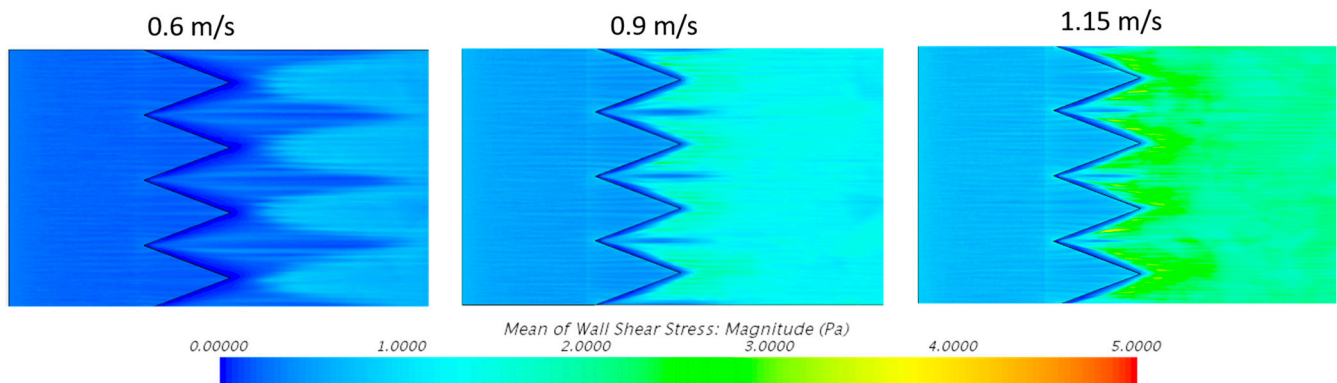
Figure 14. Contour plots of the wall shear stress magnitude from the CFD model for the three test speeds ($Re_H = 900$, 1350, and 1725) with the flow from left to right.

4.2. Flight Test Comparison

Computational wall shear stress data were compared with the flight test results [22]. Although the magnitude of the shear in the flight test is unknown, the patterns can be qualitatively compared. In addition, the patterns observed in the CFD simulations are strongly dependent on the color scale selected for the contour plots. Consequently, there was no effort made to match the results, only to see if similar trends were observed. Figure 15 shows a comparison of the diamonds from the flight scale and two CFD results. The low-shear regions at a similar height-based Reynolds number ($Re_H = U_\infty H / \nu$) show a very similar pattern (Figure 15b,c). The low-shear diamonds appear very narrow compared to the low Reynolds number case (Figure 15).
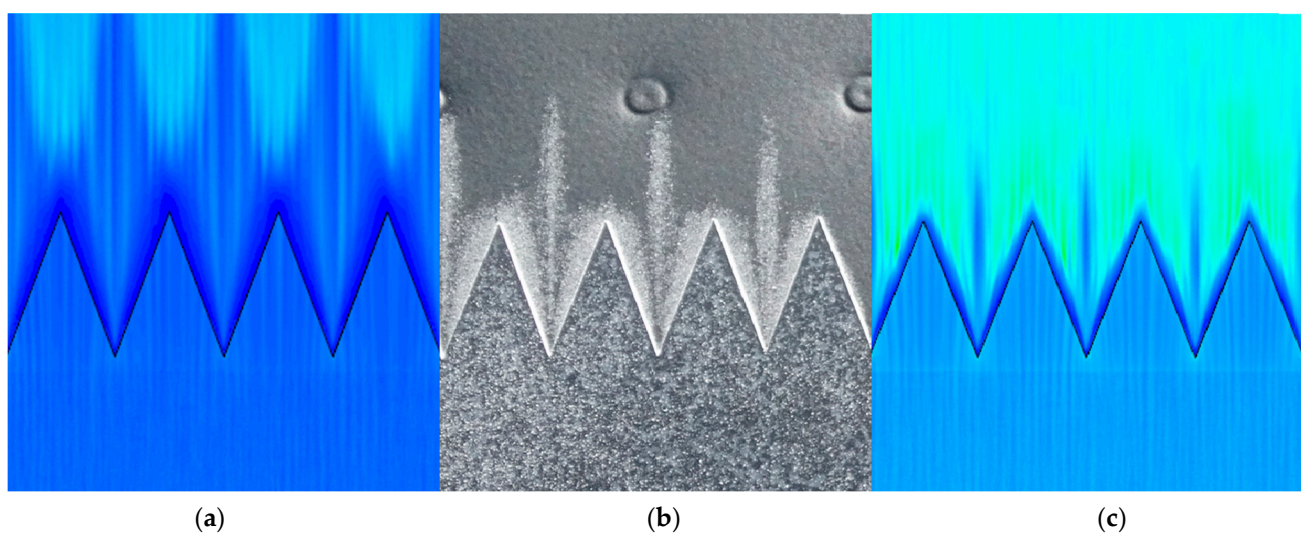

Figure 15. Wall shear stress distribution from (**a**) CFD simulation at $Re_H = 900$, (**b**) flight test [12] at $Re_H = 1360$, and (**c**) CFD at $Re_H = 1350$. Flow is from bottom to top in these images.

The flight tests [22] used several different sBFS geometries along the wing chord (see Figure 1), which provides an opportunity to examine the shear diamond dependence on the

sBFS geometry. A more in-depth analysis of the diamond size was performed by comparing the ratio of the length of the shear diamond (L_d) to the length of the sBFS geometry (L). This analysis was performed on all flight images available as well as on the simulation data. Figure 16 provides an example of how these measurements were extracted from the flight images. The shear diamond lengths were scaled with the sBFS length and plotted versus the aspect ratio (L/W) of the sBFS in Figure 16. Both the CFD and flight results were tested at three different Reynolds numbers. Error bars on the flight test data are the standard deviation from multiple sBFS measurements at the same L/W value. As previously noted, it is not surprising that the CFD and the flight scale data values do not match, even at the same Re_H, since the flight scale length is time sensitive and the CFD results are dependent on the color map. However, both the flight and CFD results have the same trend of an increase in Re_H results in a decrease in L_d/L. Furthermore, the flight test data are well approximated with a power-law fit of the form $L_d/L = C(L/W)^{-5/8}$. The constant C in the power-law function was Reynolds number dependent, with values of 3.1, 2.6, and 1.9 for $Re_H = 1360$, 1460, and 1655, respectively. Thus, inspection of the flight tests and CFD simulation shows that the low-shear diamond lengths are dependent on both the sBFS geometry (L/W) and the Reynolds number Re_H.
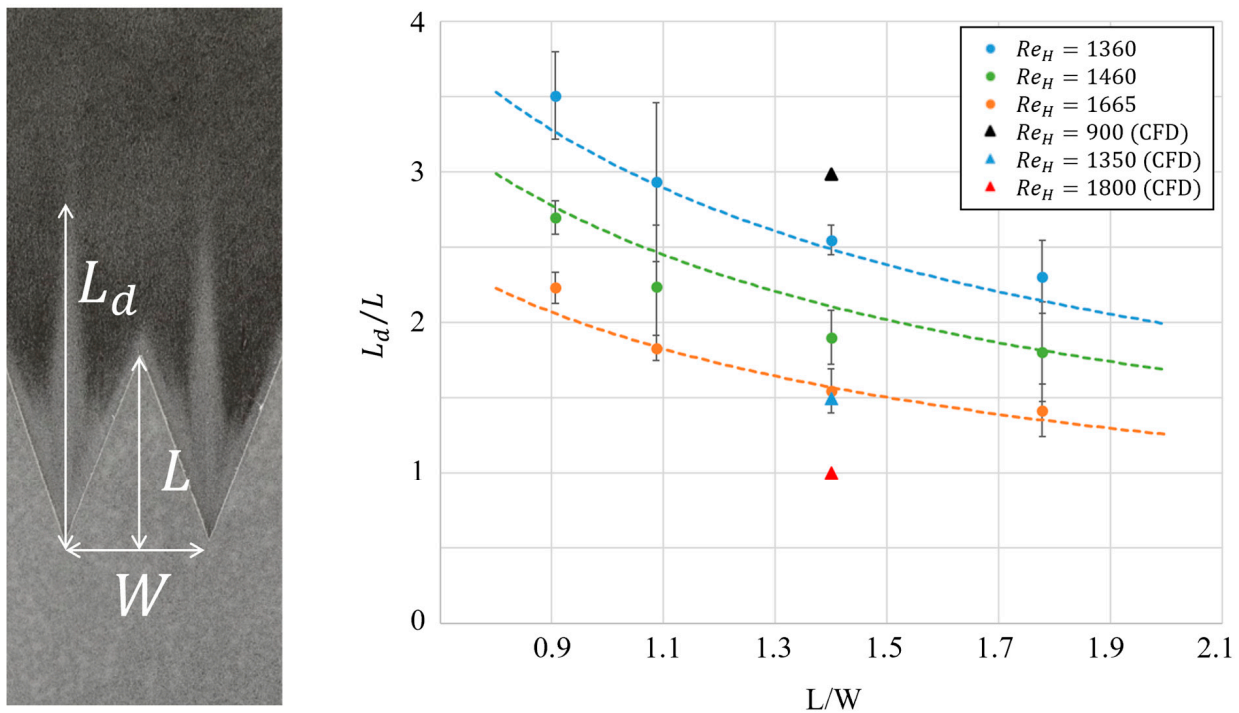

Figure 16. (**left**) A picture adapted from Kibble [22] showing the low-shear diamonds formed downstream of the sBFS on the flight test. (**right**) The shear diamond length (L_d) scaled with the sBFS length (L) plotted versus the sBFS L/W ratio at various Re_H. The dashed lines are the power-law fits for each Re_H.

4.3. Near-Wall Flow Pattern

Finally, Figure 17 shows streamlines from the computational model as they pass over the sBFS with the inlet speed at 0.6 m/s. These streamlines were seeded at the wall uniformly across the span and upstream of the sBFS. Figure 17 shows how all the near-wall flow upstream of the sBFS is directed towards the sBFS peak. Even the flow that goes over the edges between the peak and valley is then moved along the sBFS face towards the peak location. This is very similar to that observed in a similar sBFS simulation on an airfoil [25], which noted that the near-wall flow was pumped towards the peak, while flow farther from the wall showed relatively little spanwise motion. In addition, this observation is consistent with the low-shear diamonds. As the flow approaches the valley location, it is directed

towards the peaks. This results in an extended laminar region (low-shear diamond) with an immediate transition over the peaks.
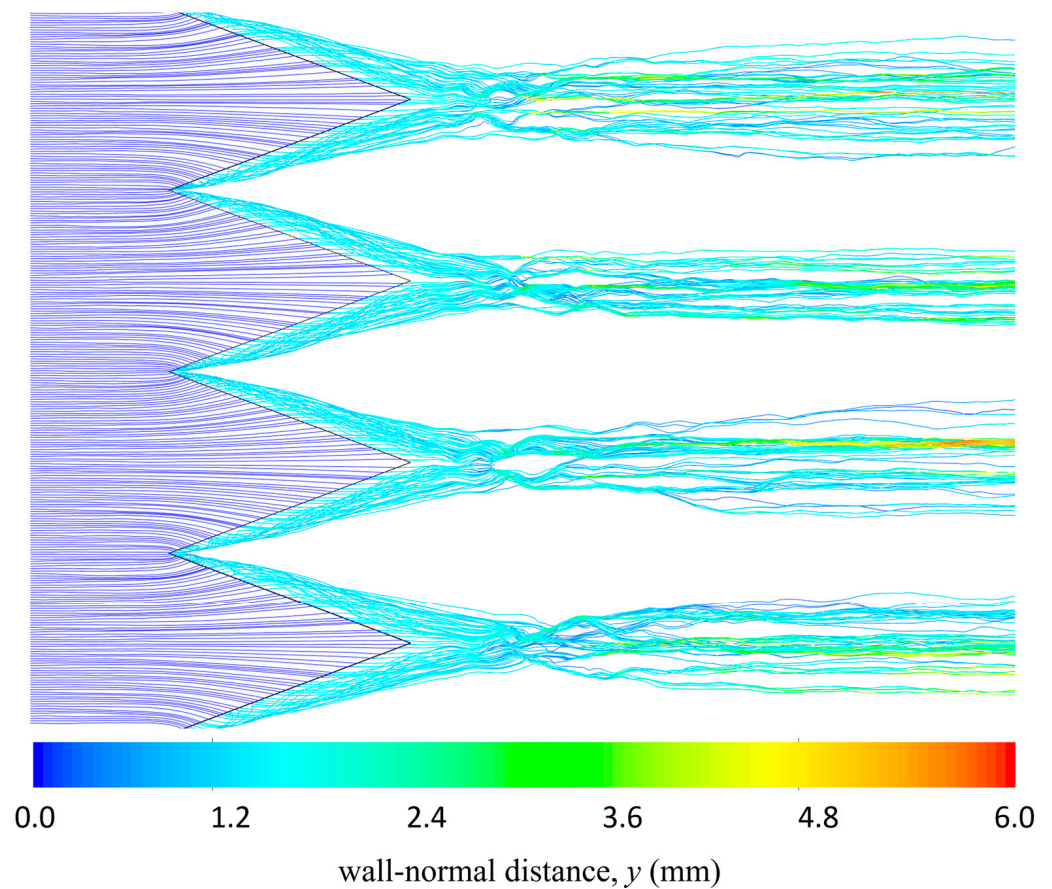

Figure 17. Streamlines that are seeded from the wall showing how the near-wall flow moves past the sBFS. The streamline color corresponds to the local distance from the wall, and the flow is from left to right.

5. Conclusions

The flow over a backward-facing step with serrations, termed an sBFS, was studied experimentally and computationally along with comparisons to observations during flight tests on a small airplane. This work proposed a scaling law for studying such problems in the subsonic regime that was able to produce experimental and computational results that were consistent with full-scale flight tests, suggesting that it was an appropriate scaling law. The low-shear diamonds observed on the flight tests were confirmed with both experiments and computational results to be the result of a delayed laminar-to-turbulent transition downstream of the valley locations of the sBFS. The length of the low-shear diamonds was shown to be proportional to sBFS geometry and the Reynolds number. Finally, the experimentally and computationally observed spanwise variation induced by the sBFS was shown to be associated with the pumping of near-wall fluid towards the downstream sBFS peak, where it would rapidly transition to turbulent flow after the step. Of note, the spanwise variation was consistent with the work of KC et al. [25] that examined the wake induced by an airfoil with a similar sBFS design to mitigate the impacts of leading-edge protective films on wind turbine blades.

References

1.   Eaton, J.K.; Johnston, J.P. A review of research on subsonic turbulent flow reattachment. *AIAA J.* **1981**, *19*, 1093–1100. [CrossRef]
2.   Goldstein, R.J.; Eriksen, V.L.; Olson, R.M.; Eckert, E.R.G. Laminar separation, reattachment, and transition of the flow over a downstream-facing step. *J. Fluids Eng.* **1970**, *92*, 732–739. [CrossRef]
3.   Chang, P.K. *Separation of Flow*; Pergamon Press: Oxford, UK, 1970.
4.   Chen, L.; Asai, K.; Nonomura, T.; Xi, G.; Liu, T. A review of Backward-Facing Step (BFS) flow mechanisms, heat transfer and control. *Therm. Sci. Eng. Prog.* **2018**, *6*, 194–216. [CrossRef]
5.   Bolgar, I.; Scharnowski, S.; Kahler, C.J. Passive Flow Control for Reduced Load Dynamics Aft of a Backward-Facing Step. *AIAA J.* **2019**, *57*, 120–131. [CrossRef]
6.   Armaly, B.F.; Durst, F.; Pereira, J.C.F.; Schönung, B. Experimental and theoretical investigation of backward-facing step flow. *J. Fluid. Mech.* **1983**, *127*, 473–496. [CrossRef]
7.   Steinthorsson, E.; Liou, M.-S.; Povinelli, L.A.; Arnone, A. Numerical simulation of three-dimensional laminar flow over a backward facing step; Flow near side walls. In Proceedings of the ASME Fluids Engineering Division Summer Meeting, ICOMP-93-21, Washington, DC, USA, 20–24 June 1993.
8.   Major, D.; Palacios, J.; Maughmer, M.; Schmitz, S. A numerical model for the analysis of leading-edge protection tapes for wind turbine blades. *J. Phys. Conf. Ser.* **2020**, *1452*, 012058. [CrossRef]
9.   Major, D.; Palacios, J.; Maughmer, M.; Schmitz, S. Aerodynamics of leading-edge protection tapes for wind turbine blades. *Wind. Eng.* **2021**, *45*, 1296–1316. [CrossRef]
10. Agrim, S.; Sapre, C.A.; Selig, M.S. Effects of leading-edge protection tape on wind turbine blade performance. *Wind. Eng.* **2012**, *36*, 525–534.
11. Gerla, M.; Kleinrock, L. Flow control: A comparative survey. *IEEE Trans. Commun.* **1980**, *28*, 553–574. [CrossRef]
12. Kostas, J.; Soria, J.; Chong, M. Particle image velocimetry measurements of a backward-facing step flow. *Exp. Fluids* **2002**, *33*, 838–853. [CrossRef]
13. Storms, B.L.; Jang, C.S. Lift enhancement of an airfoil using a Gurney flap and vortex generators. *J. Aircr.* **1994**, *31*, 542–547. [CrossRef]
14. Yao, C.; Lin, J.; Allen, B. Flowfield measurement of device-induced embedded streamwise vortex on a flat plate. In Proceedings of the 1st Flow Con-trol Conference, St. Louis, MO, USA, 24–26 June 2002.
15. Fransson, J.H.; Talamelli, A.; Brandt, L.; Cossu, C. Delaying transition to turbulence by a passive mechanism. *Phys. Rev. Lett.* **2006**, *96*, 064501. [CrossRef] [PubMed]
16. Shahinfar, S.; Sattarzadeh, S.S.; Fransson, J.H.; Talamelli, A. Revival of classical vortex generators now for transition delay. *Phys. Rev. Lett.* **2012**, *109*, 074501. [CrossRef] [PubMed]
17. Siconolfi, L.; Camarri, S.; Fransson, J.H. Boundary layer stabilization using free-stream vortices. *J. Fluid. Mech.* **2015**, *764*, R2. [CrossRef]
18. Babinsky, H.; Li, Y.; Ford, C.W.P. Microramp control of supersonic oblique shock-wave/boundary-layer interactions. *AIAA J.* **2009**, *47*, 668–675. [CrossRef]

19. Chu, H.B.; Zhang, B.Q.; Chen, Y.C. Controlling flow separation of high lift transport aircraft with micro vortex generators. *J. Northwestern Polytech. Univ.* **2011**, *29*, 799–805.

20. Paruchuri, C.; Joseph, P.; Ayton, L.J. On the superior performance of leading edge slits over serrations for the reduction of aerofoil interaction noise. In Proceedings of the 2018 AIAA/CEAS Aeroacoustics Conference, Atlanta, GA, USA, 25–29 June 2018; p. 3121.

21. Yagiz, B.; Kandil, O.; Pehlivanoglu, Y.V. Drag minimization using active and passive flow control techniques. *Aerosp. Sci. Technol.* **2012**, *17*, 21–31. [CrossRef]

22. Kibble, G.A. Experimental and Computational Investigation of the Conformal Vortex Generator. Master's Thesis, Oklahoma State University, Stillwater, OK, USA, 2017.

23. Mishnaevsky, L., Jr.; Hasager, C.B.; Bak, C.; Tilg, A.M.; Bech, J.I.; Rad, S.D.; Fæster, S. Leading edge erosion of wind turbine blades: Understanding, prevention and protection. *Renew. Energy* **2021**, *169*, 953–969. [CrossRef]

24. Scholbrock, A. *Power Performance Results UsingWind Turbine Blade Enhancing Devices Developed by Edge Aerodynamix*; Technical Report; National Renewable Energy Laboratory: Golden, CO, USA, 2017.

25. KC, R.J.; Wilson, T.C.; Alexander, A.S.; Jacob, J.D.; Lucido, N.A.; Elbing, B.R. Evaluation of a Serrated Edge to Mitigate the Adverse Effects of a Backward-Facing Step on an Airfoil. *Inventions* **2023**, *8*, 160. [CrossRef]

26. Lucido, N.A.; KC, R.; Wilson, T.C.; Jacob, J.D.; Alexander, A.S.; Elbing, B.R.; Ireland, P.; Black, J.A. Laminar Boundary Layer Scaling Over a Conformal Vortex Generator. In Proceedings of the AIAA Scitech 2019 Forum, San Diego, CA, USA, 7–11 January 2019. [CrossRef]

27. Wilson, T.C.; KC, R.; Lucido, N.A.; Elbing, B.R.; Alexander, A.S.; Jacob, J.D.; Ireland, P.; Black, J.A. Computational Investigation of the Conformal Vortex Generator. In Proceedings of the AIAA Scitech 2019 Forum, San Diego, CA, USA, 7–11 January 2019. [CrossRef]

28. Drela, M. XFOIL Subsonic Airfoil Development System. 2018. Available online: http://web.mit.edu/drela/Public/web/xfoil/ (accessed on 31 May 2024).

29. Patel, V. Calibration of the Preston tube and limitations on its use in pressure gradients. *J. Fluid. Mech.* **1965**, *23*, 185–208. [CrossRef]

30. Schlichting, H.; Gersten, K. *Boundary-Layer Theory*, 9th ed.; Springer: Berlin, Germany, 2018.

31. Wieneke, B. PIV uncertainty quantification from correlation statistics. *Meas. Sci. Technol.* **2015**, *26*, 074002. [CrossRef]

32. Shams, A.; Roelofs, F.; Komen, E.M.J.; Baglietto, E. Quasi-direct numerical simulation of a pebble bed configuration, Part I: Flow (velocity) field analysis. *Nucl. Eng. Des.* **2013**, *263*, 473–489. [CrossRef]

33. Shams, A.; Roelofs, F.; Komen, E.M.J.; Baglietto, E. Quasi-direct numerical simulation of a pebble bed configuration, Part-II: Temperature field analysis. *Nucl. Eng. Des.* **2013**, *263*, 490–499. [CrossRef]

34. Kundu, P.K.; Cohen, I.M.; Dowling, D.R. *Fluid Mechanics*, 6th ed.; Academic Press: Cambridge, MA, USA, 2016.

35. White, F.M.; Corfield, I. *Viscous Fluid Flow*; McGraw-Hill: New York, NY, USA, 2006; Volume 3.